Computational study of flow incidence effects on the aeroacoustics of low blade-tip Mach number propellers

Aerospace Science and Technology 120 (2022) 107275

Contents lists available at ScienceDirect

Aerospace Science and Technology

www.elsevier.com/locate/aescte

Computational study of flow incidence effects on the aeroacoustics of low blade-tip Mach number propellers

Gianluca Romani *, Edoardo Grande, Francesco Avallone, Daniele Ragni, Damiano Casalino

Delft University of Technology, Kluyverweg 1, 2629HS, Delft, the Netherlands

ARTICLE INFO

Article history:
Received 31 July 2021
Received in revised form 25 November 2021
Accepted 2 December 2021
Available online 7 December 2021
Communicated by Yongle Du

Keywords:
Lattice-Boltzmann method
Propeller
Drone
Yaw angle
Aerodynamics
Aeroacoustics

ABSTRACT

This paper presents a computational study of flow incidence effects on the aeroacoustics of a propeller operating at low blade-tip Mach numbers. The numerical flow solution is obtained by using the Lattice-Boltzmann/Very Large Eddy Simulation method, while far-field noise is computed through the Ffowcs-Williams & Hawkings' acoustic analogy applied on the propeller surface. The presence of an angular inflow leads to: (i) the radiation of tonal loading noise along the propeller axis; (ii) the increment/reduction of the sound pressure level in the region from/to which the propeller is tilted away/towards. However, contrarily to propellers operating at high blade-tip Mach numbers, the noise directivity change is found to be governed only by the rise of periodic unsteady loadings, with the modulation of the strength of the noise sources on the blade, associated to the periodic variation of the observer-source relative Mach number (in the blade reference frame), being negligible. Finally, thickness noise and turbulent boundary-layer trailing-edge noise did not show a significant directivity variation due to the propeller yaw angle change.

1. Introduction

The use of small-to-medium size fully-electric flying vehicles in large metropolitan areas, from drones and Unmanned Aerial Vehicles (UAVs) for goods delivery to Personal Aerial Vehicles (PAVs) for people mobility, is envisaged in the near future as a solution to roads congestion [1,2]. A number of different electrically propelled Vertical Take-Off and Landing (eVTOL) vehicles have been recently prototyped by several companies and research centers [3–7]. Most of them feature a common key characteristic, namely distributed electric propulsion systems consisting of low-speed thrust vectoring rotors/propellers, with radius below 0.5 m and blade-tip Mach number $\approx 0.2-0.5$. However, several aspects need to be addressed in order to make possible the implementation of this new technology in the upcoming years. In particular, those related to noise pollution play a primary role upon the public acceptance of Urban Air Mobility/Advanced Air Mobility (UAM/AAM), as this emerging class of flying vehicles aims at operating in close proximity of densely populated areas, where noise annoyance towards the community needs to be contained [8]. Since such vehicles are supposed to fly at relatively low forward flight velocities for which airframe self-noise is not a primarily concern [9], rotors/propellers self and installation noise are expected to be the most dominant sources of acoustic nuisance [9].

It is well known that propellers generate both broadband and tonal (harmonic) acoustic signatures [9]. The interaction of the blades with the turbulence in the incoming flow, the potential separation of the flow on the blade and the scattering of the turbulent flow at the trailing-edge of the blade are typically recognized as the most relevant mechanisms of broadband noise [10,11]. Concerning the tonal component, steady and unsteady blade aerodynamic loadings (in the blade-fixed reference frame) represent the main sources of noise at the relatively low blade-tip Mach numbers [12]. The steady loading noise is associated to the steady (in the blade-fixed reference frame) blade pressure distribution, which results in a force that periodically varies direction and generates sound for an observer in an inertial reference frame as the blade rotates [12]. For propellers operating at low blade-tip Mach numbers, this may be a relatively weak source of noise in the presence of unsteady loading noise. The latter takes place when the propeller operates in a non-uniform inflow or is set at a yaw angle, which results in a periodic and/or impulsive change of the local blade angle of attack. Examples of unsteady loading noise are the blade-vortex interaction noise or the noise generated by a propeller when it operates with the axis misaligned with respect to the free-stream direction [12]. The focus of the present study is on this last noise generation mechanism for propeller operating at low blade-tip Mach numbers.

* Corresponding author.
E-mail address: g.romani@tudelf.nl (G. Romani).

https://doi.org/10.1016/j.ast.2021.107275

During the takeoff, landing and conversion stages of the profile mission, when eVTOLs/drones generally fly in closer proximity to the ground, a propeller can operate with its shaft at a non-zero yaw angle. Under such conditions, the acoustic field radiated by the propeller may significantly differ from that of the same propeller at zero yaw angle, with a general noise increase (reduction) in the region with respect to which the propeller is tilted away (towards), resulting in a non-axisymmetric directivity pattern [13–16]. Previous computational studies on high-speed propellers attributed this asymmetry of the noise field to a periodic variation of the blade incidence, which gives rise to unsteady loading components and alters the rate of momentum injection at the blade surface, and to an in-plane convective effect, for which the efficiency of a generic acoustic source on the blade periodically varies along the azimuth [17]. The most relevant research (to the authors' knowledge) on the modeling, prediction and characterization of the aeroacoustics of propeller at incidence is outlined in the following.

A method for rotating steady line sources (acoustically compact), accurate to the first order in the in-plane Mach number, was formulated by Mani [16]. He included, in a frequency domain far-field method, the effect of the propeller yaw angle on the radiation of both the steady loading and thickness noise, in addition to that of the unsteady loading. He was the first to point out that, for highly-loaded high-speed propellers with large number of blades, the changes in the azimuthal asymmetry of the noise were more affected by a non-axisymmetric modulation of the steady loading/thickness noise due to the in-plane velocity component than by the once-per-rev unsteady loading variation.

An extension of Mani's work to high yaw angles was carried out by Krejsa [18]. He demonstrated that modeling additional yaw angle effects, such as the source motion along the free-stream velocity vector direction and the blade loading direction variation, in addition to the blade loading magnitude variation, significantly improved the comparison with the experimental data. In addition, he showed that the inclusion of higher order effects of the yaw angle (i.e. higher modes in the frequency domain far-field method as a way to remove the small yaw angle limitation of Mani's approach) changed the predicted noise at far forward and aft angles, while it had small impact near the propeller plane.

Envia [19] proposed a frequency domain formulation based on a moving-medium variant of the Ffowcs-Williams & Hawkings' equation to predict the noise from a propfan operating at incidence. His approach involved the use of the Airy's function and its derivatives, as alternative to numerical integration, and incorporated both in-plane convective effects and loading unsteadiness with no limitations on the source chordwise compactness, showing a rather favorable agreement with the experimental data.

Hanson [20] developed far-field noise formulas by applying the free-space Green's function for the convected wave equation to loading noise point sources for a propeller tilted at any angle to the flight direction. He showed that the inflow angle influences the noise through the rise of efficient radiation modes associated to the unsteady loading, and introduced the concept of *wobbling modes*, according to which the radiation efficiency of the modes changes during the rotation due to the variation of the Mach number of the sources relative to the observer.

The noise generated by a propeller in an angular inflow was numerically computed by Frota et al. [21] by using a time-domain Ffwocs-Williams & Hawkings' acoustic analogy applied on unsteady blade pressure measurements, who confirmed once again the role of both the unsteady loadings and kinematic/acoustic sources strength amplification on the variation of noise radiated by a high-speed propeller at incidence.

More recently, Roger and Moreau [22] proposed an analytical model for loading noise based on the free-space Green's function and an expansion of the fluctuating forces on the blades as circular distributions of acoustic dipoles, and computed airframe installation and propeller disk angle of attack effects on the tonal noise of a quadrotor. By considerations based on the Bessel's functions, they stressed that, for low blade-tip Mach numbers and low number of blades, unsteady-loading noise can potentially exceed that associated to the steady lift, due to the considerably higher efficiency of the 1/rev blade loading harmonics compared to that of the steady loading, even at relatively low levels of angular inflow.

Although a number of computational and experimental aeroacoustic studies have been conducted by several authors in the past on angular inflow installation effects, most of those were focused on high-speed propellers. On the one hand, experimental campaigns did not provide a thorough understanding of the change of the noise mechanisms when a propeller is operated at incidence with respect to the free-stream. On the other hand, previous computational aeroacoustic studies (mostly based on analytical models or acoustic analogies) focused only on the investigation of deterministic phenomena (i.e. periodic unsteady loadings and in-plane convective effects), and did not include in the analysis the potential change of stochastic noise generation mechanisms such as turbulent boundary-layer trailing-edge noise. Moreover, for propellers operated at low blade-tip Mach number, the kinematic/acoustic source strength modulation might not play a role as relevant as for high-speed propellers, due to the relatively low in-plane velocity periodic variation typically experienced by their blades compared to propellers operated at higher blade-tip Mach numbers. Hence, previous research can only be considered as a first step towards a better understanding of the noise radiation mechanisms of low-speed propellers at non-zero yaw angles, which is essential to drive the design of quieter UAM/AAM vehicles and satisfy noise certification regulations and environmental concerns [8].

In view of the above, the present work aims at numerically investigating the impact of non-axial inflow conditions on the tonal and broadband noise radiated by a low blade-tip Mach number propeller, as well as at providing differences of the underlying physics with respect to high-speed propellers. The Lattice-Boltzmann/Very-Large Eddy Simulation (LB/VLES) method is employed to simulate flow around a two-bladed drone propeller. The aerodynamic noise generated by the propeller is then estimated by using an acoustic analogy based on Farassat's formulation 1A of the Ffowcs-Williams & Hawkings' (FW-H) equation applied to the propeller surface. The numerical findings are supported by the validation of the numerical setup against loads and noise measurements carried out at Delft University of Technology (TU-Delft).

The article is organized as follows. In Sec. 2 an overview of the LBM/VLES approach along with the far-field noise computation method is provided. The propeller geometry and computational setup used in this study are described in Sec. 3. The validation of the computational setup is briefly outlined in Sec. 4, while the discussion on angular inflow effects on the aerodynamics and aeroacoustics of low blade-tip speed propellers is reported in Sec. 5. The main findings and conclusions of this work are summarized in Sec. 6.

2. Computational method

2.1. Flow solver

The CFD/CAA solver SIMULIA PowerFLOW® 6-2019 is used in this study to compute the flow around the propeller and extract the resulting noise signature. It is based on the Lattice-Boltzmann Method (LBM) with a wall-modeled Very Large Eddy Simulation (VLES) approach used for turbulence modeling [23–30]. PowerFLOW® solves the Boltzmann equation for the distribution function $f(\mathbf{x}, t, \mathbf{v})$, which represents the probability to find, in the

elementary volume d$\mathbf{x}$ around the spatial position $\mathbf{x}$ and in the infinitesimal time interval $(t, t + \mathrm{d}t)$, a number of fluid particles with velocity in the interval $(\mathbf{v}, \mathbf{v} + \mathrm{d}\mathbf{v})$. The Boltzmann equation is solved by discretizing the space velocity domain into a prescribed number of values in magnitude and direction. For low-subsonic flow simulations, the D3Q19 model is used, which employs 19 velocity states in the 3 spatial dimensions [31]:

$$f_i(\mathbf{x} + \mathbf{v}_i \Delta t, t + \Delta t) - f_i(\mathbf{x}, t) = C_i(\mathbf{x}, t), \tag{1}$$

where f_i represents the particle distribution function along the i-th direction, according to the finite set of discrete velocities ($\mathbf{v}_i$: i = 0,..., 18), and $\mathbf{v}_i \Delta t$ and Δt are the space and time increments, respectively. In Eq. (1), the collision term C_i is modeled with the Bhatnagar-Gross-Krook (BGK) approximation [31,32]:

$$C_i(\mathbf{x}, t) = -\Delta t/\tau [f_i(\mathbf{x}, t) - f_i^{eq}(\mathbf{x}, t)], \tag{2}$$

where τ is the relaxation time parameter, which is related to the fluid dimensionless kinematic viscosity and temperature, and f_i^{eq} is the equilibrium distribution function, which approximated through a third order Hermite polynomial expansion and related to local hydrodynamic properties [31]. Hydrodynamic flow quantities, such as flow density and velocity, can be determined through the zero-th and first order moments of the discrete distribution function [25], respectively, whereas all the other physical quantities can be determined through ideal gas thermodynamics.

The LBM scheme is solved on a Cartesian grid composed of cubic volumetric elements (Voxels). The surface of solid bodies is discretized within each voxel intersecting the wall geometry using planar surface elements (Surfels). A boundary scheme based on a particle bounce-back process and a specular reflection process is used to reproduce no-slip and slip wall boundary conditions [33], respectively. For simulations of rotating geometries, the computational domain is decomposed into an outer ground-fixed reference frame and an inner body-fixed Local Reference Frame (LRF). The latter is characterized by a mesh which rigidly rotates with the rotating geometry so that no relative motion between the LRF grid and the enclosed geometry occurs. An external body force term, corresponding to the inertial force introduced by the non-inertial rotating LRF, is introduced at the right hand side of the discrete Boltzmann equation for the fluid region inside the LRF domain [34]. A closed transparent interface is used between the inner and outer domains in order to connect the two fluid flow regions [35].

2.2. Far-field noise solver

A hybrid CFD/CAA approach is adopted to compute the far-field noise in order to avoid expensive computations associated to the necessity of accurately resolving the acoustic waves propagation up to the far-field directly in the CFD simulation. Specifically, a Ffowcs-Williams and Hawkings' (FW-H) acoustic analogy [36] is used to compute the far-field noise from the knowledge of the body geometry, kinematics, and surface pressure distribution. The FW-H solver used in this work (*Opty∂B*-PFNOISESCAN by Dassault Systèmes) is based on a forward-time solution [37] of Farassat's formulation 1A [38]. It includes surface distributions of acoustic monopoles and dipoles, typically referred to as thickness and loading terms, while neglecting the volume/quadrupole term, which would account for all the possible non-linear effects in the volume surrounding the integration surface (i.e. shock waves, turbulence mixing and propagation effects). This last source term is expected to be negligible for low-speed propellers due to the low blade-tip Mach number M [12]. For a subsonically moving solid surface S, far-field noise is thus computed as the superposition of thickness noise (p'_T), associated to the fluid displacement due to the body motion, and loading noise (p'_L), due to the forces exerted by the body on the surrounding fluid, namely $p'(\mathbf{x}, t) = p'_T(\mathbf{x}, t) + p'_L(\mathbf{x}, t)$, where:

$$4\pi\, p'_T(\mathbf{x}, t) = \int_S \left[\frac{\rho_0 \dot{v}_n}{r\,(1 - M_r)^2}\right]_{\mathrm{ret}} \mathrm{d}S(\mathbf{y}) + \int_S \left[\frac{\rho_0\, v_n \left(r\dot{M}_r + c_0\left(M_r - M^2\right)\right)}{r^2\,(1 - M_r)^3}\right]_{\mathrm{ret}} \mathrm{d}S(\mathbf{y}) \tag{3}$$

$$4\pi\, p'_L(\mathbf{x}, t) = \frac{1}{c_0}\int_S \left[\frac{\dot{L}_r}{r\,(1 - M_r)^2}\right]_{\mathrm{ret}} \mathrm{d}S(\mathbf{y}) + \int_S \left[\frac{L_r - L_M}{r^2\,(1 - M_r)^2}\right]_{\mathrm{ret}} \mathrm{d}S(\mathbf{y}) + \frac{1}{c_0}\int_S \left[\frac{L_r \left(r\dot{M}_r + c_0\left(M_r - M^2\right)\right)}{r^2\,(1 - M_r)^3}\right]_{\mathrm{ret}} \mathrm{d}S(\mathbf{y}) \tag{4}$$

In the above equations, $\mathbf{r} = \mathbf{x} - \mathbf{y}$ is the radiation vector between the observer $\mathbf{x}$ and source $\mathbf{y}$ positions, $\boldsymbol{v}$ and $\mathbf{M} = \boldsymbol{v}/c_0$ are the velocity and Mach number of a source point on the body surface S, c_0 and ρ_0 are the undisturbed speed of sound and flow density, $r = |\mathbf{r}|$ and $M = |\mathbf{M}|$. In addition, $\mathbf{L} = (p - p_0)\hat{\mathbf{n}}$ is the source point loading vector, with p and p_0 being the surface and undisturbed pressure, respectively, and $\hat{\mathbf{n}}$ represents the outward surface unit normal vector. Furthermore, dots on quantities denote time derivatives with respect to the source time t_{ret} (differing from the observer time t) observed in a reference frame fixed with undisturbed medium, while the subscripts r and n denote the projections along the radiation and surface normal directions, respectively.

3. Propeller geometry and computational setup

The geometry used in this study (shown in Fig. 1(a)) is a two-bladed propeller designed at TU-Delft and derived from an APC 9x6 propeller. It is characterized by a radius R of 0.15 m and NACA 4412 airfoil sections, which are merged with the propeller hub by elliptical sections (for $r < 0.01$ m). The airfoil chord and twist spanwise distributions are shown Fig. 1(b). The propeller hub radius is 1.25 cm and connected to a nacelle of 5 cm diameter and 52 cm length. The propeller geometry under examination has been experimentally tested in the A-Tunnel of TU-Delft and will be used for future low-Reynolds number propeller benchmarking [39,40]. Fig. 1(a) shows the free-stream (x_f, y_f, z_f) and the ground-fixed (x_g, y_g, z_g) reference frames. The propeller axis coincides with the x-axis of the ground-fixed reference frame (x_g), while the azimuthal position of the blade ψ is referred to its z-axis (z_g). The free-stream reference frame is rotated by the propeller yaw angle α around the y-axis (y_g) of the ground-fixed one. The free-stream velocity V_∞ is directed along the x-axis of the former in such a way that the free-stream velocity vector is decomposed into axial V_{x_∞} and in-plane velocity V_{z_∞} components in the ground-fixed coordinate system, respectively. The propeller is operated at fixed angular velocity ($n = 83.33$ rps, i.e. $\omega = 523.6$ rad/s) and free-stream velocity of 10 m/s, resulting in an advance ratio $J = 0.4$ (where $J = V_\infty/(nD)$, with n denoting the revolution per seconds and D the propeller diameter). The resulting tip Mach number is 0.23 and the Reynolds number based on the chord at 75% of the radius is about $9 \cdot 10^4$. Two different values of the propeller yaw angle are considered to investigate the effects of an angular inflow, namely $\alpha = 0°$ and 15°. The free-stream static pressure and

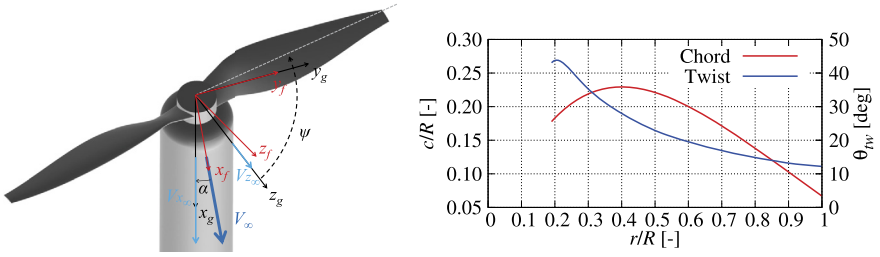

(a) *Propeller and coordinate systems* (b) *Airfoil chord and twist distributions*

Fig. 1. Propeller geometry, coordinate systems, airfoil chord and twist spanwise distributions. (For interpretation of the colors in the figure(s), the reader is referred to the web version of this article.)

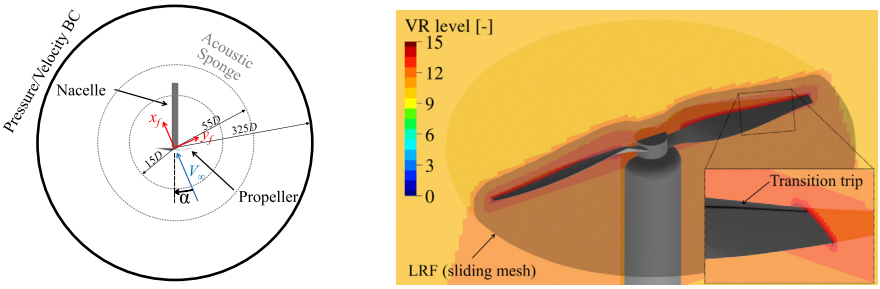

(a) *Computational setup* (b) *Near body mesh*

Fig. 2. Sketch of (a) computational setup (not drawn to scale) and (b) near body mesh.

temperature considered are $p_\infty = 99000$ Pa and $T_\infty = 293.15$ K, respectively.

Fig. 2(a) illustrates the computational setup used in this study. The computational fluid domain is a spherical volume of $325D$ radius centered around the propeller. Free-stream static pressure and velocity, and turbulence intensity of 0.1% of the free-stream velocity are prescribed on its outer boundary. The experimental anechoic wind tunnel geometry is not modeled in the computational setup. Consequently, the sound is propagated in free-field. An acoustic sponge is used to dissipate the out-going acoustic waves and minimize the backward reflection from the outer boundary and reproduce a digital anechoic environment. The acoustic sponge is defined by two concentric spheres of radius $15D$ and $55D$, respectively, centered around the propeller. The fluid kinematic viscosity is gradually increased starting from its physical value within the inner sphere, up to an artificial value two orders of magnitude higher outside the outer one. A zig-zag transition trip is employed on the suction side of the blade to drive the LBM/VLES scheme switching from turbulence modeling to scale-resolving behavior, thus allowing the formation of resolved turbulent structures within the boundary-layer for the sake of turbulent boundary-layer trailing-edge noise broadband calculation. The zig-zag trip is characterized by a thickness of 0.17 mm, amplitude and wavelength of 0.9 mm, and is placed at 25% of the chord on the suction side of the blade for $r/R > 0.2$ (Fig. 2(b)). No trip is placed on the blade pressure side, since no laminar-to-turbulent boundary layer transition is expected to occur based on BEMT/2D viscous panel method computations. This approach has been successfully validated in previous studies carried out by the authors for the prediction of the performances and tonal/broadband noise radiation of a low-speed propeller in axial inflow conditions [39,41].

Fig. 2(b) shows the details of the computational setup and mesh in proximity of the propeller geometry. The propeller and hub are encompassed by a volume of revolution that defines the Local Reference Frame (LRF), namely the rotating sliding mesh domain used to reproduce the propeller rotation. The solid FW-H integration surface used to compute the far-field noise radiation coincides with the propeller, hub and nacelle surfaces. A total of 16 Variable Resolution (VR) regions are used to discretize the whole fluid domain, with the finest resolution level (VR15) placed around the blade trip and trailing-edge. A resolution of 200 voxels along the mean chord (22.85 mm) is used in the second finest resolution level (VR14), resulting in a smallest voxel size of 0.06 mm, a mean $y+ \approx 5$ on the blade surface and an overall mesh size of 107 million voxels. The computational cost is 840 CPUh/rev on a 430 cores cluster with Intel Xeon CPU E5-2697 2.6 GHz. The whole fluid domain is initialized with the instantaneous flow solution from a statistically converged coarser simulation. Hence, after a settling time corresponding to 2 propeller revolutions, the sampling of relevant flow data is started for 10 additional revolutions. Acoustic data is sampled at 365 kHz with spatial averaging of 0.5 mm on the solid FW-H integration surface. Fourier transformed data is obtained with 2 Welch blocks, 50% overlap and Hanning windowing, corresponding to a bandwidth of 16.6 Hz (BPF 0.1).

4. Numerical setup validation

The grid independence and the validation of the numerical setup under axial inflow conditions have been carried out in previous studies by the authors [39,41]. In this section, the numerical results are compared against forces and noise measurements carried out in the A-Tunnel of TU-Delft to validate the employed computational setup for angular inflow cases. No transition trip was employed in the experimental data reported. A more detailed discussion on the yaw effects on propeller loads and noise will follow in Sec. 5.

4.1. Mean thrust, torque and propulsive efficiency coefficients

The comparison between the time-averaged experimental and numerical thrust (C_T) and torque (C_Q) coefficients, and propulsive efficiency (η) at the two different propeller yaw angles ($\alpha = 0°$ and

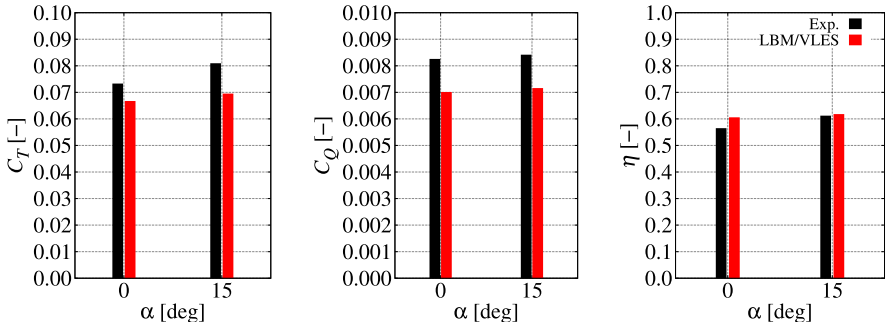

Fig. 3. Thrust (left), torque (center) and propulsive efficiency (right) coefficients variation with the propeller yaw angle α.

15°) is shown in Fig. 3. C_T, C_Q and η are computed as follows, respectively:

$$C_T = \frac{T}{\rho n^2 D^4}, \quad C_Q = \frac{Q}{\rho n^2 D^5} \quad \text{and} \quad \eta = \frac{J C_T}{2\pi C_Q}, \tag{5}$$

where T and Q are the mean propeller thrust and torque, n is the number of revolutions per second and D is the propeller diameter. Note that the uncertainty of the measuring instruments is about 0.1% and 0.05% of the measured thrust and torque values, respectively. Moreover, the experimental uncertainty due to the variability of the propeller rotational speed is about 0.6% for the thrust and 0.03% for the torque [40]. From Fig. 3, a certain under-prediction of thrust and torque coefficients can be observed for both axial ($\alpha = 0°$) and angular ($\alpha = 15°$) inflow conditions. A previous study carried out by the authors, for the same propeller operated at zero incidence with respect to the free-stream, suggested that the presence of the trip (which is used to generate resolved turbulent pressure fluctuations in the boundary-layer for trailing-edge noise generation) can be the cause for such discrepancies [41]. Conversely, the propulsive efficiency results to be predicted in a more satisfactory way, as the aforementioned under-prediction of C_T and C_Q tend to cancel out in the computation of η. Interestingly, the increase of thrust, torque and efficiency coefficients with the increase of the propeller yaw angle is also captured by the numerical simulations, although to a lower extent with respect to the experimental data variation.

4.2. Far-field noise spectra

After the assessment of the thrust and torque predictions, the capability of the numerical setup to capture the effect of the propeller yaw angle on both its tonal and broadband acoustic signatures is hereinafter analyzed. Two different microphones in the free-stream coordinate system are considered: Mic. 7 (0.0 m, 1.2 m, 0.0 m) and Mic. 11 (-0.75 m, 1.2 m, 0.0 m), respectively located in and out of the propeller plane (for $\alpha = 0°$), as depicted in Fig. 4. The corresponding far-field noise spectra are reported in Figs. 5 and 6, respectively. Results are reported in 1/12-octave band sound pressure spectrum $L_{p(1/12)}$ versus the frequency f normalized by the Blade-Passing Frequency (BPF = $n_f B$ = 167 Hz, with n_f the shaft frequency in Hz and B the number of blades). In each figure, two different microphones array positions are considered, namely array 1 and array 2, away from and towards which the propeller is respectively tilted for non-zero α. For each microphone, the unloaded (i.e. without the propeller) electric motor noise (in orange) and the background noise (in green) of the wind tunnel are reported to further support the discussion. Note that the background noise always refers to the $\alpha = 0°$ condition and that the same numerical and experimental spectra are shown on arrays 1 and 2 for the axial flow conditions, due to the axial symmetry of noise radiation. Moreover, it worth mentioning that the main

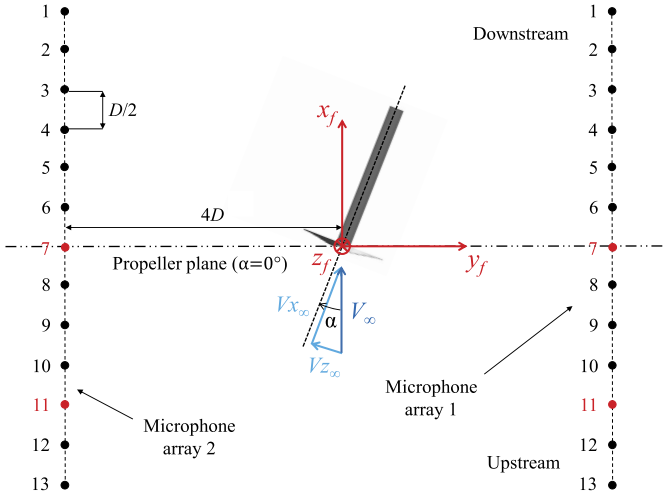

Fig. 4. Sketch of the microphone array used of far-field noise computation (drawn not to scale).

sources of experimental uncertainty are represented by: (i) the background noise below wind tunnel cut-off frequency (∼200 Hz), which is responsible for the large broadband noise levels at low frequency; (ii) the imperfect balance of the blade loading and the loaded electric motor noise that cause the rise of harmonics of the shaft frequency (BPF 0.5, 1, 1.5, etc.); and (iii) the unloaded electric motor noise, which generally adds mid-frequency tonal contributions (approximately between BPF 5 to 25) to the far-field noise spectrum [39,40]. The uncertainty of the GRAS40PH free-field microphones used in the experiment is about 1 dB, from 50 Hz to 5 kHz, and 2 dB, from 5 kHz to 20 kHz, while the BPF 1 tone level uncertainty due to variations of the rotational speed was found to be about 1 dB [40].

The prediction of tonal and broadband noise is quite satisfactory for both axial ($\alpha = 0°$) and angular ($\alpha = 15°$) inflow conditions. For what concerns harmonic noise, the tone at BPF 1 is quite well predicted within 2-3 dB under-prediction depending on the observer position considered. Such a moderate mismatch of the BPF 1 tone, might be attributed to the lower thrust and torque predictions observed in the numerical prediction (Fig. 3), whose impact is estimated to be around 1.5 dB based on BEMT/FW-H compact monopole/dipole computations, as well as to the experimental imperfect balance of the blade loading (that leads to the generation of harmonics of the shaft frequency) and the wind-tunnel acoustic confinement effect at low frequency (i.e. test chamber not completely anechoic below 200 Hz). Nevertheless, the expected increment of tonal noise at BPF 1 in that region from which the propeller is tilted away (array 1), as well as the reduction of noise in the opposite region (array 2), are well captured by the numerical setup. A similar behavior is also observed for the tone at BPF

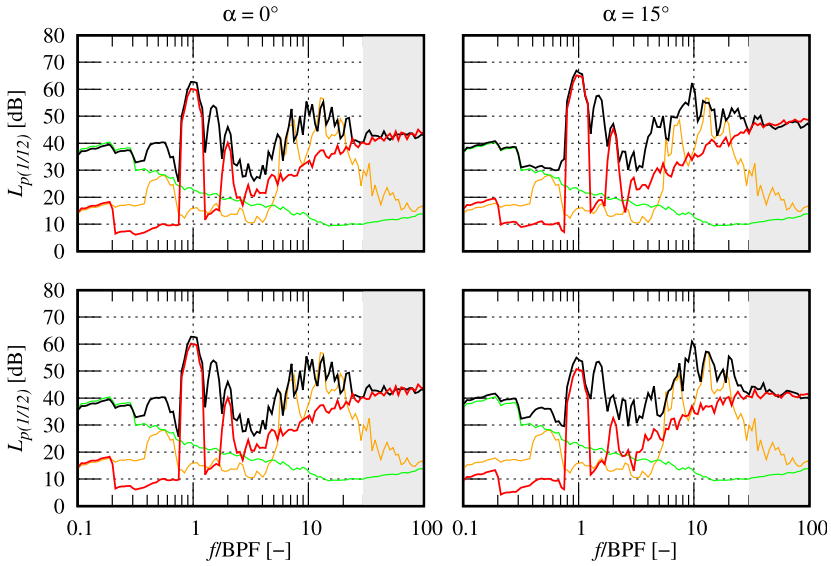

Fig. 5. Far-field noise sound pressure level in 1/12-octave band $L_{p(1/12)}$ variation with the propeller yaw angle α for Mic. 7; array 1 (top) and array 2 (bottom). Experiment (—), LBM/VLES (—), electric motor noise (—) and wind tunnel background noise (—).

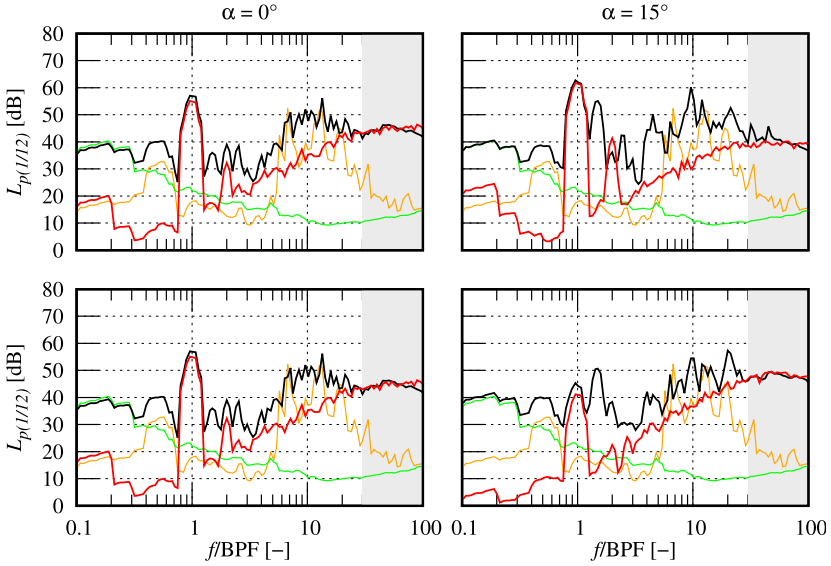

Fig. 6. Far-field noise sound pressure level in 1/12-octave band $L_{p(1/12)}$ variation with the propeller yaw angle α for Mic. 11; array 1 (top) and array 2 (bottom). Experiment (—), LBM/VLES (—), electric motor noise (—) and wind tunnel background noise (—).

2 in the numerical results, with a noise increment on array 1 and a reduction on array 2. However, this trend is not uniquely found in the experimental data. Possible reasons for such an unexpected behavior might be related to the presence of spurious tonal noise components at low frequency harmonics of the shaft rotation (BPF 0.5, 1, 1.5, etc.), which could be relevant when compared to the weak BPF 2 tone to such an extent to considerably affect its variation with the propeller yaw angle change.

Regarding the broadband noise, levels are very well predicted for frequencies lying between BPF 30 and 100 (highlighted by the grey rectangle). For intermediate frequencies (BPF 5 to 25), the experimental electric motor noise dominates the noise levels due to turbulent boundary-layer trailing-edge noise, and no direct assessment of the numerical results against the experimental data can be drawn. Interestingly, the employed computational approach, which is based on the use of a zig-zag transition trip to promote the generation of resolved pressure fluctuations within the boundary-layer that are scattered as sound at the blade trailing-edge, is able to capture the moderate changes of the broadband noise levels at high frequency due to the change of the propeller yaw angle. Such variations are less pronounced compared to those occurring to the tones at the first two BPFs, and do not follow the same trends manifested by the tonal components. More specifically, Mic. 7 on the array 1 shows some high-frequency broadband noise increment for $\alpha = 15°$ (Fig. 5) and almost no variation on the array 2, compared to the axial flow case ($\alpha = 0°$). Conversely, for Mic. 11 (Fig. 6), a slightly reduction and increment of the broadband noise component can be respectively noted on the arrays 1 and 2, when the propeller is operated at incidence.

5. Analysis of angular inflow effects

5.1. Velocity and angle of attack distributions

In order to correlate the effect of the propeller yaw angle on the blade aerodynamic loading variations, the flow experienced by

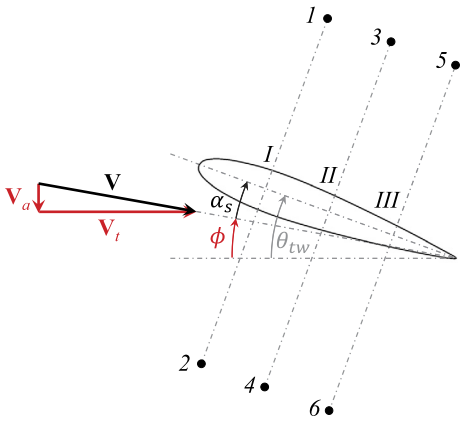

Fig. 7. Sketch of the 3-points method for the local airfoil angle of attack extraction [42,43].

a propeller blade during a revolution is investigated first. Fig. 8 shows the axial (V_a) and tangential (V_t) velocity components and angle of attack (α_s) for $\alpha = 0°$, as well as their variations ($\Delta V_a = V_{a,15°} - V_{a,0°}$, $\Delta V_t = V_{t,15°} - V_{t,0°}$ and $\Delta\alpha_s = \alpha_{s,15°} - \alpha_{s,0°}$) under angular inflow conditions ($\alpha = 15°$), experienced by the different blade sections along a propeller revolution. The azimuthal coordinate ψ indicates the blade position on the propeller disk (see Fig. 1(a)), while the radial coordinate represent the spanwise section location normalized by the propeller radius, r/R. The circular and straight arrows indicate the direction of the rotational velocity and in-plane free-stream (cross-flow) velocity for the tilted propeller, respectively.

The extraction of the sectional angle of attack from phase-locked averaged simulation data is carried out following the *3-points* method proposed by Rahimi et al. [42,43]. It consists in extracting, for each radial section and blade azimuthal position, the velocity vectors (in the non-inertial reference frame rigidly rotating with the blade) in correspondence of six points, three located on the suction side (1, 3 and 5) and three on the pressure side (2, 4 and 6) at 25, 50 and 75% of the chord at a distance of approximately one chord away from the local airfoil aerodynamic center in the normal direction (Fig. 7). For each couple of points at the three different chordwise locations (I, II and III), the velocities are averaged by using an interpolating function (arithmetic mean in the present work), resulting in three velocity vectors for each station: $\mathbf{V}_I = (\mathbf{V}_1 + \mathbf{V}_2)/2$, $\mathbf{V}_{II} = (\mathbf{V}_3 + \mathbf{V}_4)/2$ and $\mathbf{V}_{III} = (\mathbf{V}_5 + \mathbf{V}_6)/2$. Then, the velocity vector perceived by the local airfoil is computed as arithmetic average of the three previous velocities, $\mathbf{V} = (\mathbf{V}_I + \mathbf{V}_{II} + \mathbf{V}_{III})/3$, and decomposed into axial and tangential components to extract the induction angle ϕ that, subtracted to the blade geometrical twist θ_{tw}, provides the local airfoil angle of attack: $\alpha_s = \theta_{tw} - \phi = \theta_{tw} - \tan^{-1}(V_a/V_t)$.

For the propeller operating at zero yaw angle, the axial and tangential velocity components and the local airfoil angle of attack show the expected axisymmetric pattern, with dependency on the radial coordinate only, and constant values along the azimuth. In particular, the axial velocity component (Fig. 8(a)) is increased by the propeller rotation up to 40% of its undisturbed value for $0.4 < r/R < 0.8$, whereas the tangential component (Fig. 8(c)) and the sectional angle of attack (Fig. 8(e)) increase and decrease, respectively, along the blade span.

Regarding the case with the propeller at incidence, more interesting results can be found. First, Fig. 8(d) shows the expected result that, when the propeller is operated at incidence with respect to the free-stream, the tangential velocity component experienced by the local airfoil section is increased on the blade advancing side ($0° < \psi < 180°$) and decreased on the retreating one ($180° < \psi < 360°$), due to the rise of an in-plane free-stream velocity component. Less foreseeable is the variation of the axial velocity component induced by the non-zero propeller yaw angle, which shows spanwise maxima and minima roughly in correspondence of $\psi = 45°$ and $\psi = 225°$, respectively. The advancing side of the blade is mostly characterized by an increment of the axial velocity, while the opposite phenomenon occurs on the retraining side. However, the axial and tangential velocity components variation do not appear to be in phase, with the former being 30° delayed with respect to the latter. As previously pointed out, the combination of both axial and tangential sectional velocities defines the local airfoil angle of attack (Fig. 7), whose variation for $\alpha = 15°$ is shown in Fig. 8(f). In particular, an increment of the axial velocity is responsible for a reduction of the local angle of attack experienced by the blade, whereas an increase in the tangential velocity results in higher α_s. This explains why the blade angle of attack is not purely increasing (decreasing) on the blade advancing (retreating) side when the propeller is at incidence, rather it shows a periodic variation with a phasing of about 30-45° delay with respect to the ideal blade angle of attack variation (i.e. that based on the tangential velocity only).

5.2. Unsteady thrust and torque distributions

Next, the influence of the propeller yaw angle on the unsteady loading is investigated. Fig. 9 shows the sectional thrust ($C_{\partial_r T}$) and torque ($C_{\partial_r Q}$) coefficient (per unit span) distributions for $\alpha = 0°$, as well as their variations ($\Delta C_{\partial_r T} = C_{\partial_r T,15°} - C_{\partial_r T,0°}$ and $\Delta C_{\partial_r Q} = C_{\partial_r Q,15°} - C_{\partial_r Q,0°}$) for $\alpha = 15°$, of a single propeller blade as functions of the azimuth and radial coordinate. The thrust and torque coefficients distributions are computed as follows:

$$C_{\partial_r T} = \frac{\partial_r T}{\rho n^2 D^3} \quad \text{and} \quad C_{\partial_r Q} = \frac{\partial_r Q}{\rho n^2 D^4}, \tag{6}$$

where $\partial_r T = \partial T/\partial r$ and $\partial_r Q = \partial Q/\partial r$ represent the blade thrust and torque per unit span, respectively. For the axial inflow case, the thrust and torque distributions shows axisymmetric distributions over the rotor disk with the highest values around 80% of the radial coordinate (Figs. 9(a) and 9(b)). The root and tip regions generate a lower amount of sectional thrust due to the relatively lower flow velocity and tip-vortex induced lift deficit, respectively. Similar considerations can be drawn for the torque for inboard blade sections (Fig. 9(b)). Conversely, the outer part of the blade shows a lower relative torque reduction compared to that observed for the thrust, due to the fact that the former is equally dependent from the local airfoil pressure distribution and skin friction through the sectional drag.

When the propeller axis is tilted with respect to the free-stream velocity component, both the section thrust and torque distributions exhibit a periodic variation along the blade azimuth, with the highest and lowest values reached slightly after $\psi = 90°$ and $\psi = 270°$, respectively. Such unsteady loading variations are not perfectly in phase with that of the tangential velocity component (which dominates the total velocity change perceived by the blade sections), due to its dependence from the sectional angle of attack as well. For $\alpha = 15°$, the sectional thrust and torque coefficients increments on the blade advancing side are larger than their corresponding reductions occurring on the retreating one. This is further highlighted in Fig. 10 for three spanwise locations ($r/R = 0.6, 0.7, 0.9$), which shows the ratio between the sectional thrust and torque coefficient (per unit span) between the yawed and axial cases. Specifically, it can be observed that the increment of sectional thrust and torque on the advancing side is roughly two times larger than the corresponding reduction occurring on the retreating one. This aspect can explain the moderate increase of the

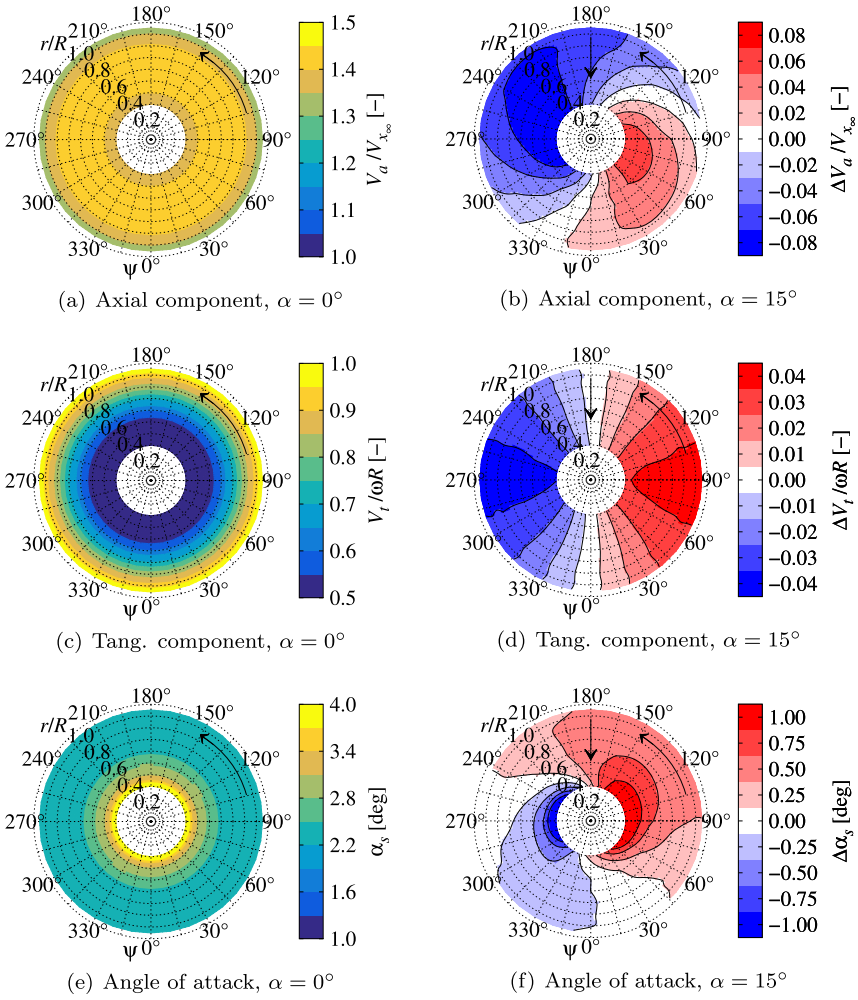

(a) Axial component, $\alpha = 0°$ (b) Axial component, $\alpha = 15°$

(c) Tang. component, $\alpha = 0°$ (d) Tang. component, $\alpha = 15°$

(e) Angle of attack, $\alpha = 0°$ (f) Angle of attack, $\alpha = 15°$

Fig. 8. Axial and tangential velocity components and angle of attack distributions for axial flow ($\alpha = 0°$) and their variations under angular inflow conditions ($\alpha = 15°$).

mean thrust and torque coefficients observed in Fig. 3 and is primarily related to the larger local airfoil angle of attack increase on the advancing side compared to its reduction taking place on the retreating one. Moreover, this phenomenon is expected to take place to a larger extent in the experiment, due to the larger increment of C_T and C_Q observed in the measurements when the propeller is at incidence. The use of a zig-zag transition trip in the computational setup, which is known to slightly reduce the pressure suction effect at the blade leading-edge [41], might have limited the occurrence of the aforementioned phenomenon in the numerical simulation.

5.3. Far-field noise directivity

The far-field noise directivities in the plane of the propeller (y_g-z_g plane) and along its axis (x_g-z_g plane) are respectively shown in Figs. 11 and 13 for both the axial ($\alpha = 0°$) and angular ($\alpha = 15°$) inflow cases. These are computed on two circular arrays of $10R$ radius centered on the propeller hub and composed by 25 evenly spaced microphones. The circular and straight arrows in Fig. 11 indicate the propeller angular velocity and the free-stream in-plane velocity component directions, while the straight arrow in Fig. 13 represents the free-stream velocity vector direction. The propeller is sketched in grey in each plot. For both the in-plane and out-of-plane directivities, the total far-field noise (in red) is further decomposed into its thickness (in green) and loading (in blue) components according to Eqs. (3) and (4), respectively. The far-field noise directivity is presented in terms of Sound Pressure Level (SPL), with the root-mean-square of the acoustic pressure integrated over three different blade-passing frequency ranges: BPF 0.1-100, BPF 1 and BPF 10-100. The former is representative of the overall sound pressure level (hence, hereinafter defined as OASPL) directivity around the propeller. Moreover, as it can be inferred from Figs. 5 and 6, the latter is a measure of the directivity associated to the broadband component of the noise dominated by the turbulent boundary-layer trailing-edge noise, while the SPL around BPF 1 provides information about the directivity of the tonal noise at the most dominant harmonic.

Previous research pointed out that the effect of the propeller yaw angle on the far-field noise radiation has a twofold nature: one aerodynamic, related to the rise of unsteady loading sources, and one kinematic or acoustic, associated to the phase modulation of the strength of all the sources due to a periodic variation of the observer-source relative Mach number (for an observer rigidly rotating with the blade) [20,17]. For low-speed propellers, the first mechanism is still relevant because of the high radiation efficiency of the unsteady loading modes [22]. Contrarily, the kinematic/acoustic effect may play a minor or negligible role due to the relatively low free-stream Mach, and consequently of its in-plane component responsible for the source strength modulation. The relative importance of this effect for $\alpha = 15°$ is investigated in this work by performing FW-H computations without the free-stream cross-flow velocity component, whose corresponding total

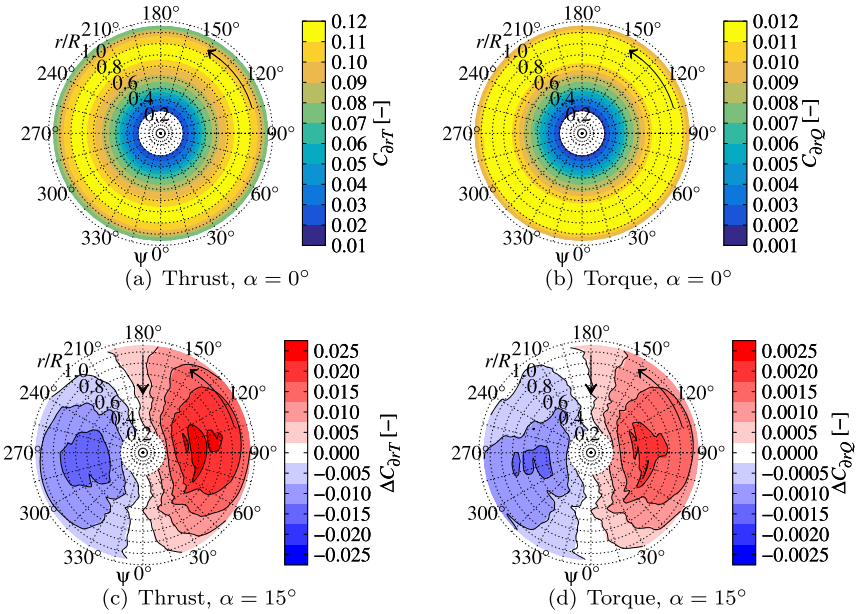

Fig. 9. Thrust and torque coefficients (per unit span) distributions for axial flow ($\alpha = 0°$) and their variations under angular inflow conditions ($\alpha = 15°$).

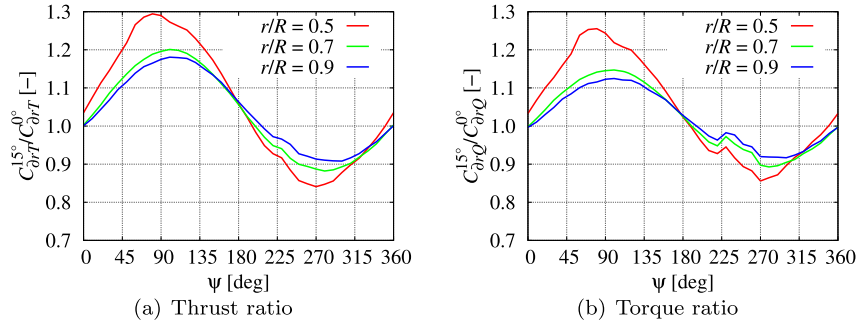

Fig. 10. Ratio of the thrust and torque coefficients between $\alpha = 15°$ and $\alpha = 0°$ cases for three spanwise locations.

far-field noise directivities are depicted by the black crosses in Figs. 11 and 13.

5.3.1. In-plane noise directivity

For axial inflow conditions ($\alpha = 0°$), the far-field noise shows the expected axisymmetric in-plane directivity for all the three frequency ranges considered. The tonal noise at BPF 1 (Fig. 11(c)) contributes the most to the overall sound pressure level (Fig. 11(a)) in the plane of the propeller compared to the broadband component (Fig. 11(e)). Moreover, the loading noise represents the most important contributor to the total acoustic pressure for all the frequency ranges considered. While for the SPL at BPF 1 thickness noise is still relatively important when compared to loading noise (Figs. 11(c) and 11(d)), the latter is the only relevant contributor to noise in the BPF range 10-100 (Figs. 11(e) and 11(f)). However, it should be pointed out the different nature of these loading noise sources for the two different frequency ranges. At the BPF 1, the loading noise is associated to the presence of steady forces generated by the rotating blades in a frame that is not inertial with respect to a far-field observer. Conversely, the broadband noise in the frequency range BPF 10-100 is due to the presence of stochastic unsteady loadings in the reference frame rigidly connected to the blade. Such non-deterministic unsteady loadings are those related to the turbulent pressure fluctuations in the boundary-layer over the blade suction side which are scattered as sound at the blade trailing-edge.

Similar considerations can be inferred for the case with the propeller axis at an angle with respect to the free-stream velocity direction ($\alpha = 15°$), except for the axial symmetry of the noise directivity, which is significantly altered by the presence of a cross-flow velocity component. In line with previous studies [13–16], the total far-field noise is increased in that region from which the propeller is tilted away ($90° < \phi < 270°$) and decreased in the opposite one ($270° < \phi < 90°$). However, this noise directivity change is only related to the generation of periodic blade unsteady loadings (shown in Fig. 9), due to the periodic variation of the incidence and velocity experienced by the blade. Indeed, FW-H computations without the cross-flow velocity components (black crosses in Figs. 11(b), 11(d) and 11(f)) provides almost identical results to those in which the in-plane convective effects are considered, thus implying that the aforementioned kinematic/acoustic modulation effect of the source strength can be neglected for the case under examination. As shown in Fig. 11(d), the presence of unsteady loading of the blade is responsible for a SPL increment of the loading noise at the first BPF up to 6 dB at $\phi = 195°$, and for a reduction up to 12 dB in the diametrically opposite direction, which in turn affects the directivity of the total far-field noise. The circumferential positions of the maximum and minimum noise are located 90° ahead of the locations of maximum and minimum blade loading, respectively. This is a consequence of the fact that the noise generated by the propeller blade mainly radiates perpendicularly to it. Conversely, thickness and broadband noise are not significantly altered in the plane of rotation when the pro-

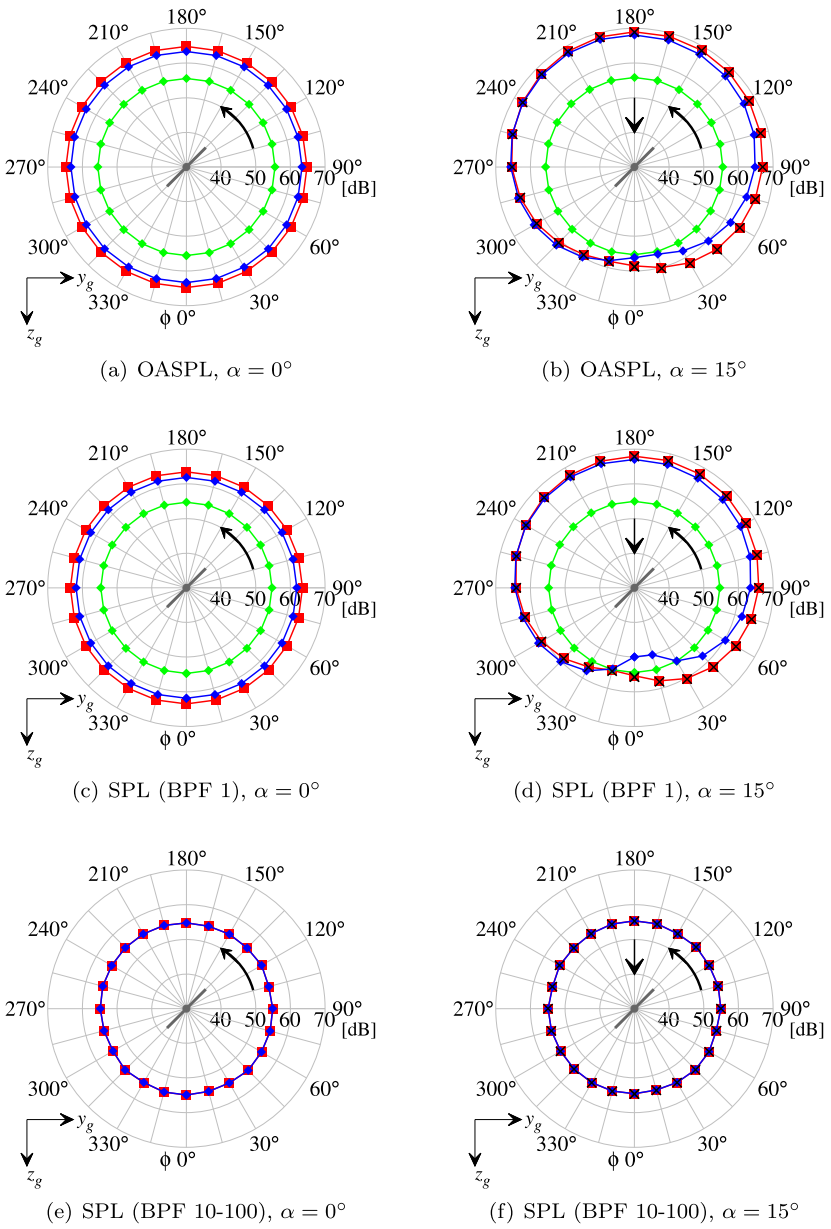

(a) OASPL, $\alpha = 0°$ (b) OASPL, $\alpha = 15°$

(c) SPL (BPF 1), $\alpha = 0°$ (d) SPL (BPF 1), $\alpha = 15°$

(e) SPL (BPF 10-100), $\alpha = 0°$ (f) SPL (BPF 10-100), $\alpha = 15°$

Fig. 11. SPL in-plane directivity of total (—■—), thickness (—◆—) and loading noise (—◆—) for $\alpha = 0°$ and $\alpha = 15°$. Total noise without cross-flow velocity component for $\alpha = 15°$ (✕).

peller is at incidence with respect to the free-stream. This can be ascribed to the relatively low periodic variations of both section angle of attack and velocity, respectively below 0.5° and 5% of the undisturbed local airfoil free-stream velocity for outboard blade sections, resulting in a negligible unsteady (in the rotor frame) flow displacement and turbulent boundary-layer properties, which respectively underlie thickness and trailing-edge noise generation.

To complement the SPL directivity plots reported in Fig. 11, Fig. 12 shows the narrow band spectra in 1/12-octave bands at two in-plane observer angles, $\phi = 0°$ and $\phi = 180°$, corresponding to the regions of maximum noise increment and reduction under yawed conditions ($\alpha = 15°$), respectively. Once again, an increment of the total noise at the first two BPFs can be observed for the observer position from which the propeller is titled away ($\phi = 180°$) with respect to the axial flow case ($\alpha = 0°$), while a noise reduction of BPF 1 and 2 takes place in the opposite region ($\phi = 0°$). Conversely, no significant broadband noise variation can be appreciated between the yawed and axial cases. It should be pointed out that such a negligible variation of the (broadband) sound pressure level within the frequency range 10-100 observed in Fig. 11 is not antithetical to the moderate high-frequency broadband changes illustrated in Figs. 5 and 6. Indeed, the far-field noise spectra in Figs. 5 and 6 are reported in 1/12-octave bands to better discern tonal noise at low frequency and broadband noise at mid- to high-frequencies. However, this leads the p'_{rms} to be integrated over frequency bands of increasing width as the frequency increases, resulting in an apparent larger contribution of higher frequencies to the overall broadband noise energy. Although not shown for the sake of brevity, the far-field noise spectra in constant frequency bands highlight a more balanced broadband energy distribution across mid and high frequencies, so that the moderate changes of the high-frequency broadband noise do not significantly influence the SPL integrated within BPF 10-100.

5.3.2. Out-of-plane noise directivity

Next, the out-of-plane (axial) noise directivity (i.e. on the x_g-z_g plane illustrated in Fig. 1(a)) is shown in Fig. 13. As a first result, it can be noticed that tonal noise propagates mainly in the

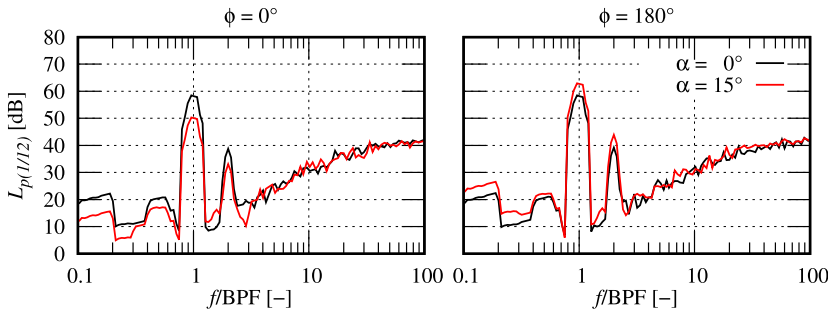

Fig. 12. Sound pressure level in 1/12-octave band $L_{p(1/12)}$ of the total noise for $\alpha = 0°$ and $\alpha = 15°$ at two different in-plane observer positions: $\phi = 0°$ and $\phi = 180°$.

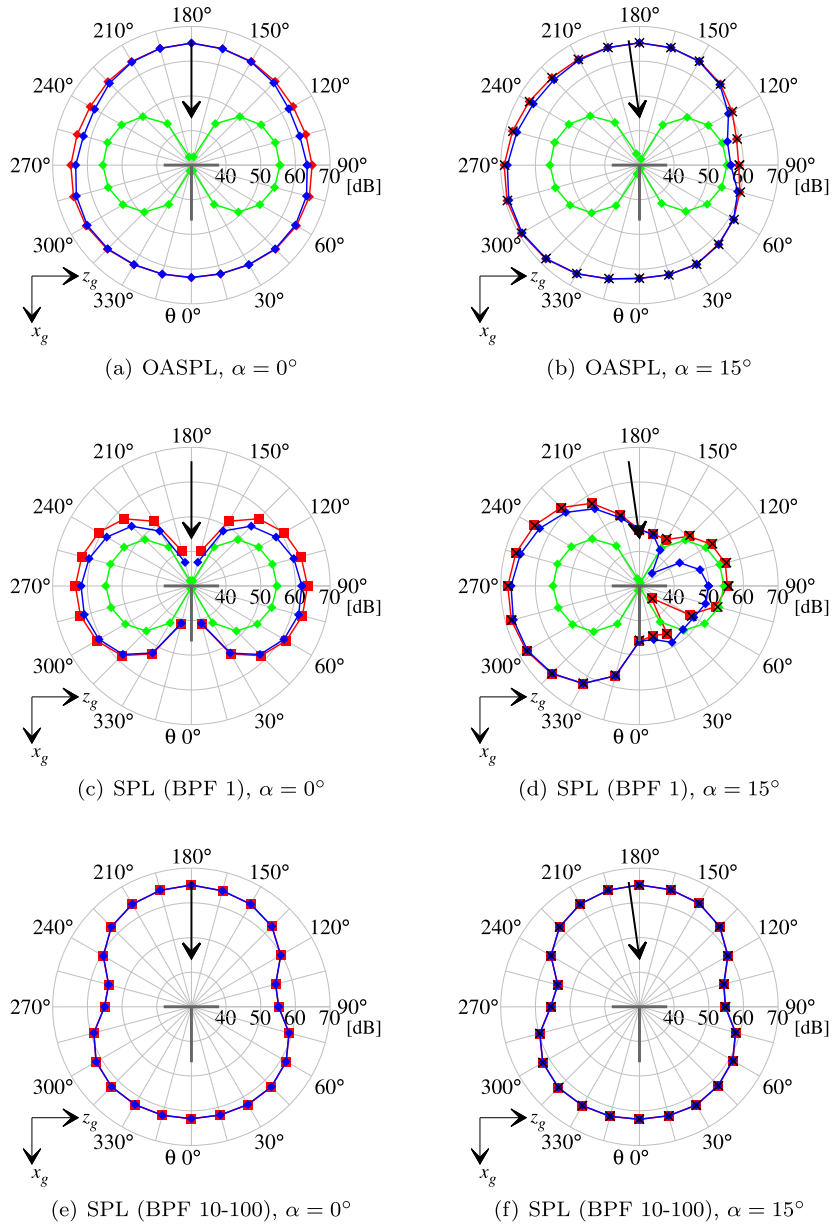

Fig. 13. SPL out-of-plane directivity of total (—■—), thickness (—◆—) and loading noise (—◆—) for $\alpha = 0°$ and $\alpha = 15°$. Total noise without cross-flow velocity component for $\alpha = 15°$ (✕).

propeller plane for axial flow conditions ($\alpha = 0°$), with almost no noise radiation occurring of along propeller axis (Fig. 13(c)), as expected. Conversely, broadband noise shows (Fig. 13(e)) a more uniform out-of-plane directivity with the largest noise levels radiated perpendicularly to the propeller plane. This is consistent with the turbulent boundary-layer trailing-edge noise theory according to which the noise radiates following a dipolar/cardiodid pattern approximately symmetric with respect to the local airfoil

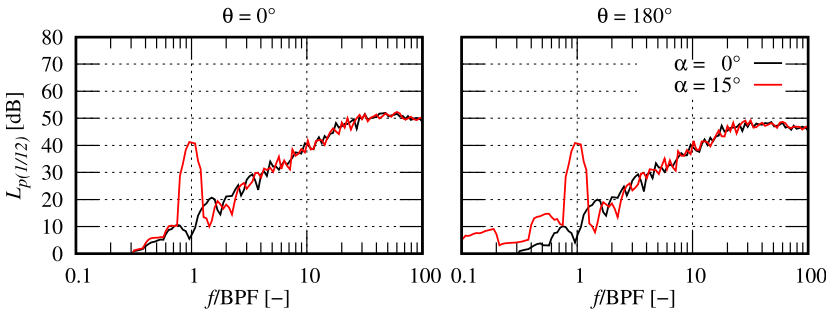

Fig. 14. Sound pressure level in 1/12-octave band $L_{p(1/12)}$ of the total noise for $\alpha = 0°$ and $\alpha = 15°$ at two different out-of-plane observer positions: $\theta = 0°$ and $\theta = 180°$.

chord [9]. As a result, both tonal and broadband noise contribute to the out-of-plane OASPL directivity (Fig. 13(a)), with the former dominating along the propeller plane, while the latter on the propeller axis.

For the propeller with a non-zero yaw angle, the OASPL along the propeller plane is increased in that area from which the propeller is tilted away and reduced in the opposite one (Fig. 13(b)), as already shown in the in-plane directivity plots. This noise directivity change is governed by the modification of the loading noise at BPF 1 (Fig. 13(d)), with broadband noise directivity modifications being negligible (Fig. 13(f)). Interestingly, loading noise at BPF 1 dramatically increases along the propeller axis, as further shown by the noise spectra in Fig. 14 for two on-axis observers above ($\theta = 180°$) and below ($\theta = 0°$) the propeller plane. This is clearly the indication of the presence of unsteady loading harmonics that, contrarily to the noise associated to the steady contribution of the force (i.e. rotor-locked noise), lead to the propagation of noise in the direction of the propeller axis. As previously shown for the in-plane directivity, convective modulation effects on the noise sources on the blade are negligible also for what concerns the radiation along the propeller axis. Finally, it is interesting to point out that, for some particular observer angles (i.e. $345° < \theta < 30°$ for in-plane observers and $45 < \theta < 150°$ for out-of-plane ones) the loading noise decreases to such an extent that thickness noise becomes the most important noise source at BPF 1 (Figs. 11(d) and 13(d)), due to the forces reduction occurring around $\psi = 270°$ (Figs. 9(c) and 9(d)).

Although not shown for the sake of conciseness, considerations similar to that derived above for the SPL at BPF 1 can be inferred for the noise directivity variation of the second BPF harmonic.

5.4. Noise power level

The survey on the propeller yaw angle effects on the resulting radiated field is concluded with the analysis of the source power level, which is representative of the acoustic energy generated by the propeller regardless the distance and the observation angle. The source Power Level (PWL) spectrum is evaluated by integration of the Power Spectral Densities (PSDs) of the (total) acoustic signature computed through the FW-H acoustic analogy over a spherical array of $10R$ radius centered around the propeller hub, using the following formula:

$$\mathrm{PWL}(f) = \int_0^{2\pi}\int_0^{2\pi} R_s^2 \sin(\theta) \frac{[1+M_0\cos(\theta)]^2 \mathrm{PSD}(f,\phi,\theta)}{2\rho_0 c_0} \mathrm{d}\phi \mathrm{d}\theta \quad (7)$$

where f is the frequency, R_s is the sphere radius, θ and ϕ are the angular coordinates defined in Fig. 11 and Fig. 13, respectively, while M_0, ρ_0 and c_0 are the free-stream Mach number, density and speed of sound. A total of 625 microphones, 25 per each angular coordinate, have been used for the PWL calculation. Fig. 15

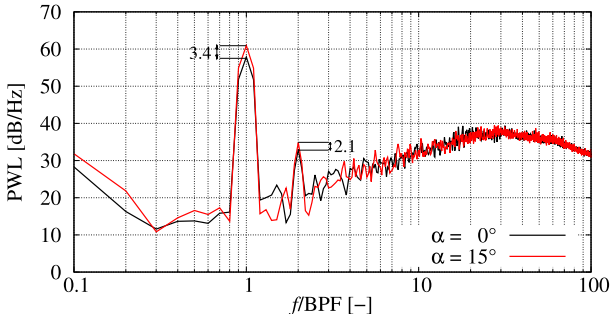

Fig. 15. Source power level variation with the propeller yaw angle.

shows, for the axial ($\alpha = 0°$) and angular ($\alpha = 15°$) inflow cases, the one-sided source power level spectrum computed using Eq. (7), with the PWL converted from W/Hz to dB/Hz considering a reference sound power $\mathrm{PWL}_{\mathrm{ref}} = 10^{-12}$ W. The PWL spectrum reveals that the source power is increased by 3.4 dB and 2.1 dB at BPF 1 and 2, respectively, when the propeller is tilted by 15° with respect to the free-stream velocity direction, regardless the presence of regions of sound pressure level increment and reduction around the propeller. Conversely, no variation of the broadband component of the source power can be appreciated, as expected from the negligible in-plane and out-of-plane sound pressure level directivity variations shown in Figs. 11 and 13.

As a final result, the sectional source power level variation with α at the first BPF is analyzed. Specifically, the two blades of the propeller are both split into ten evenly spaced strips between root and tip. Then, FW-H acoustic signals from each couple of strips at iso-radius are evaluated on the aforementioned spherical array in order to compute the contribution of each strip to the whole propeller source power. The corresponding results for BPF 1 are reported in Fig. 16 with respect to the blade section count, where 1 and 10 respectively correspond to the root and tip strips. The total source power (red) is further decomposed into thickness (green) and loading (blue) noise-related PWL contributions. Under axial inflow conditions (Fig. 16(a)), the outer part of the blade contributes the most to the far-field noise radiation, with loading noise being the dominant source of noise. As the propeller is set at incidence with respect to the free-stream velocity, the outer part of the blade is still largely responsible for the overall noise emissions, although the relative contribution of inner blade sections increases more than that associated to outer ones. This is a consequence of the fact that the innermost blade sections experience the largest loading and fluid displacement variations relative to the axial inflow case, due to the largest local angle of attack and velocity changes occurring at those spanwise locations. Similar considerations can be drawn for the BPF 2, whose results are not reported for the sake of conciseness.

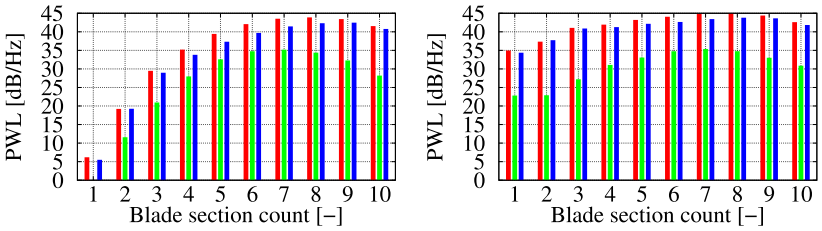

(a) BPF 1, $\alpha = 0°$ (b) BPF 1, $\alpha = 15°$

Fig. 16. Sectional source power level at BPF 1 of total (—), thickness (—) and loading (—) noise.

6. Conclusions

This paper presented a computational study on flow incidence effects on the aeroacoustics associated to low-speed propeller operated at a yaw angle with respect to the free-stream. The numerical flow solution was obtained by solving the explicit, transient and compressible lattice-Boltzmann equation implemented in the CFD/CAA solver SIMULIA PowerFLOW®. The aerodynamic noise generated by the propeller was computed by using the Farassat's formulation 1A of the FW-H equation applied to the propeller/nacelle surfaces. A transition trip was used on the suction side of the propeller blades in the computational setup to force the numerical scheme to switch from modeled to scale-resolving turbulence mode and trigger the formation of turbulent structures for the sake of turbulent boundary-layer trailing-edge noise generation.

Numerical results were compared against forces and noise measurements carried out in the A-Tunnel of TU-Delft to assess the capability of the employed computational setup to predict loads, tonal and broadband noise modifications due to a non-zero propeller yaw angle. Both absolute values and variations, due to the propeller yaw angle change, of the time-averaged thrust and torque were reasonably captured by the computational setup, although to a lower extent compared to those observed in the experimental data. A quite satisfactory agreement between numerical and experimental data was found for both tonal noise at BPF 1 and broadband noise above BPF 30, with the numerical setup able to capture the large tonal noise variation, as well as the moderate high-frequency broadband changes, at different observer locations due the modification of the propeller yaw angle.

The analysis of the velocity field for the propeller at incidence revealed a nearly symmetric variation (in absolute value) of the tangential velocity experienced by the different blade sections with respect to in-plane free-stream velocity component, with an increment on the advancing side and a reduction on the retreating one. The local angle of attack variation was found to take place with a phase shift of 30° in advance with respect to that of the tangential velocity, which dominates the total velocity experienced by the blade section, causing the unsteady aerodynamic loadings to reach the highest and lowest values slightly after $\psi = 90°$ and $\psi = 270°$, respectively. Moreover, larger sectional thrust and torque increments were observed on the blade advancing side compared to the reductions occurring on the retreating one, explaining the higher mean propeller thrust and torque coefficients found in both numerical and experimental data.

Similarly to previous studies on high-speed propellers, the effect of the propeller yaw angle on the far-field noise resulted in a large increment of the noise radiated along the propeller axis, and an increase of the sound pressure level in the region from which the propeller is tilted away and a decrease in the opposite one. However, contrarily to propeller experiencing high cross-flow Mach number components, such a noise directivity change was found to be related only to the rise of deterministic unsteady loadings on the blade due to the periodic variation of the incidence and velocity experienced by the blade. FW-H computations without the cross-flow velocity component provided nearly identical results to those in which the in-plane convective effects were considered, thus implying that the kinematic/acoustic modulation effect of the sources strength can be neglected for low-speed propellers at incidence. Finally, thickness and broadband noise did not show a significant directivity variation due to the propeller yaw angle, as a consequence of the moderate variation of the sectional angle of attack and velocity, which could have resulted in a negligible unsteady flow displacement and turbulent boundary-layer properties changes at the blade trailing-edge.

Declaration of competing interest

The authors declare that they have no known competing financial interests or personal relationships that could have appeared to influence the work reported in this paper.

References

[1] J. Holden, N. Goel, Fast-Forwarding to a Future of On-demand Urban Air Transportation, Uber Elevate White Paper, 2016.
[2] D. Casalino, W.C.P. van der Velden, G. Romani, Community noise of urban air transportation vehicles, in: Proceedings of the AIAA Scitech 2019 Forum, 2019, Paper 1834.
[3] Electric VTOL News^{TM}, VoloDrone, https://evtol.news/volocopter-volodrone/.
[4] Electric VTOL News^{TM}, A^3 Vahana, https://evtol.news/aircraft/a3-by-airbus/.
[5] Electric VTOL News^{TM}, eHang 216, https://evtol.news/ehang-216/.
[6] Electric VTOL News^{TM}, eHang 116, https://evtol.news/ehang-116/.
[7] Electric VTOL News^{TM}, Lift HEXA, https://evtol.news/lift-hexa/.
[8] M.M. Connors, Factors that Influence Community's Acceptance of Noise: An Introduction for Urban Air Mobility, NASA/TM-2019-220325, 2019.
[9] H.H. Hubbard, Aeroacoustics of Flight Vehicles: Theory and Practice. Volume 1: Noise Sources, 1991.
[10] C.E. Hughes, NASA Collaborative Research on the Ultra High Bypass Engine Cycle and Potential Benefits for Noise, Performance, and Emissions, NASA/TM-2013-216345, 2013.
[11] T. Brooks, D. Pope, M. Marcolini, Airfoil Self-Noise and Prediction, NASA Reference Publication 1218, 1989.
[12] S. Glegg, W. Devenport, Aeroacoustics of Low Mach Number Flows: Fundamentals, Analysis, and Measurement, Academic Press, 2017.
[13] P. Block, The effects of installation on single- and counter-rotation propeller noise, in: Proceedings of the 9th AIAA Aeroacoustics Conference, 1984, Paper 2263.
[14] P. Block, Experimental Study of the Effects of Installation on Single and Counter-Rotation Propeller Noise, NASA TP-2541, 1986.
[15] R. Woodward, Measured noise of a scale model high speed propeller at simulated takeoff/approach conditions, in: Proceedings of the 25th AIAA Aerospace Sciences Meeting, 1987, Paper 526.
[16] R. Mani, The radiation of sound from a propeller at angle of attack, Proc. R. Soc. Lond. Ser. A, Math. Phys. Sci. 431 (1882) (1990) 203–218, https://doi.org/10.1098/rspa.1990.0127.
[17] M. Carley, The structure of wobbling sound fields, J. Sound Vib. 244 (1) (2001) 1–19, https://doi.org/10.1006/jsvi.2000.3451.
[18] E. Krejsa, Prediction of the Noise from a Propeller at Angle of Attack, NASA Technical Memorandum 103627, 1990.
[19] E. Envia, Prediction of noise field of a propfan at angle of attack, in: Unsteady Aerodynamics, Aeroacoustics, and Aeroelasticity of Turbomachines and Propellers, Springer, 1993, pp. 685–703.
[20] D.B. Hanson, Sound from a propeller at angle of attack: a new theoretical viewpoint, Proc. R. Soc. Lond. Ser. A, Math. Phys. Sci. 449 (1936) (1995) 315–328, https://doi.org/10.1098/rspa.1995.0046.

[21] J. Frota, P. Lempereur, M. Roger, Computation of the noise of a subsonic propeller at an angle of attack, in: Proceedings of the 4th AIAA/CEAS Aeroacoustics Conference, 1998, Paper 2282.
[22] M. Roger, S. Moreau, Tonal-noise assessment of quadrotor-type UAV using source-mode expansions, Acoustics 2 (3) (2020) 674–690, https://doi.org/10.3390/acoustics2030036.
[23] V. Yakhot, S.A. Orszag, Renormalization group analysis of turbulence. I. Basic theory, J. Sci. Comput. 1 (1) (1986) 3–51, https://doi.org/10.1007/BF01061452.
[24] V. Yakhot, S.A. Orszag, S. Thangam, T.B. Gatski, C.G. Speziale, Development of turbulence models for shear flows by a double expansion technique, Phys. Fluids A 4 (7) (1992) 1510–1520, https://doi.org/10.1063/1.858424.
[25] H. Chen, S. Kandasamy, S.A. Orszag, S. Succi, V. Yakhot, Extended Boltzmann kinetic equation for turbulent flows, Science 301 (5633) (2003) 633–636, https://doi.org/10.1126/science.1085048.
[26] H. Chen, S. Orszag, I. Staroselsky, S. Succi, Expanded analogy between Boltzmann kinetic theory of fluid and turbulence, J. Fluid Mech. 519 (2004) 301–314, https://doi.org/10.1017/S0022112004001211.
[27] X. Shan, X.-F. Yuan, H. Chen, Kinetic theory representation of hydrodynamics: a way beyond the Navier-Stokes equation, J. Fluid Mech. 550 (2006) 413, https://doi.org/10.1017/S0022112005008153.
[28] R. Zhang, X. Shan, H. Chen, Efficient kinetic method for fluid simulation beyond the Navier-Stokes equation, Phys. Rev. E 74 (4) (2006) 046703, https://doi.org/10.1103/PhysRevE.74.046703.
[29] H. Chen, I. Goldhirsch, S.A. Orszag, Discrete rotational symmetry, moment isotropy, and higher order lattice Boltzmann models, J. Sci. Comput. 34 (1) (2008) 87–112, https://doi.org/10.1007/s10915-007-9159-3.
[30] H. Chen, R. Zhang, P. Gopalakrishnan, Filtered lattice Boltzmann collision formulation enforcing isotropy and Galilean invariance, Phys. Scr. 95 (3) (2020) 034003.
[31] H. Chen, S. Chen, W. Matthaeus, Recovery of the Navier-Stokes equations using a lattice-gas Boltzmann method, Phys. Rev. A 45 (8) (1992) 5339–5342, https://doi.org/10.1103/PhysRevA.45.R5339.
[32] P.L. Bhatnagar, E.P. Gross, M. Krook, A model for collision processes in gases. I. Small amplitude processes in charged and neutral one-component systems, Phys. Rev. 94 (3) (1954) 511–525, https://doi.org/10.1103/PhysRev.94.511.
[33] H. Chen, C. Teixeira, K. Molvig, Realization of fluid boundary conditions via discrete Boltzmann dynamics, Int. J. Mod. Phys. C 9 (8) (1998) 1281–1292, https://doi.org/10.1142/S0129183198001151.
[34] R. Zhang, C. Sun, Y. Li, R. Satti, R. Shock, J. Hoch, H. Chen, Lattice Boltzmann approach for local reference frames, Commun. Comput. Phys. 9 (5) (2011) 1193–1205, https://doi.org/10.4208/cicp.021109.111110s.
[35] G. Tabor, A.D. Gosman, R.I. Issa, Numerical simulation of the flow in a mixing vessel stirred by a Rushton turbine, in: Institution of Chemical Engineers Symposium Series, vol. 140, Citeseer, 1996, pp. 25–34.
[36] J.E. Ffowcs-Williams, D.L. Hawkings, Sound generated by turbulence and surfaces in arbitrary motion, Philos. Trans. R. Soc. Lond. Ser. A 264 (1151) (1969) 321–342, https://doi.org/10.1098/rsta.1969.0031.
[37] D. Casalino, An advanced time approach for acoustic analogy predictions, J. Sound Vib. 261 (4) (2003) 583–612, https://doi.org/10.1016/S0022-460X(02)00986-0.
[38] F. Farassat, G.P. Succi, The prediction of helicopter discrete frequency noise, Vertica 7 (4) (1983) 309–320.
[39] D. Casalino, E. Grande, G. Romani, D. Ragni, F. Avallone, Definition of a benchmark for low Reynolds number propeller aeroacoustics, Aerosp. Sci. Technol. 113 (2021) 106707, https://doi.org/10.1016/j.ast.2021.106707.
[40] E. Grande, G. Romani, D. Ragni, F. Avallone, D. Casalino, Aeroacoustic investigation of a propeller operating at low-Reynolds number, AIAA J. (2021), https://doi.org/10.2514/1.J060611, Article in Advance.
[41] G. Romani, E. Grande, F. Avallone, D. Ragni, D. Casalino, Performance and noise prediction of low-Reynolds number propellers using the lattice-Boltzmann method, Aerosp. Sci. Technol. (2021) 107086, https://doi.org/10.1016/j.ast.2021.107086, in press.
[42] H. Rahimi, M. Hartvelt, J. Peinke, J.G. Schepers, Investigation of the current yaw engineering models for simulation of wind turbines in BEM and comparison with CFD and experiment, J. Phys. Conf. Ser. 753 (2) (2016) 022016, https://doi.org/10.1088/1742-6596/753/2/022016.
[43] H. Rahimi, J. Schepers, W.Z. Shen, N.R. García, M.S. Schneider, D. Micallef, C.J.S. Ferreira, E. Jost, L. Klein, I. Herráez, Evaluation of different methods for determining the angle of attack on wind turbine blades with CFD results under axial inflow conditions, Renew. Energy 125 (2018) 866–876, https://doi.org/10.1016/j.renene.2018.03.018.